

Beyond Perfect Scores: Proof-by-Contradiction for Trustworthy Machine Learning

Dushan N. Wadduwage*
 Old Dominion University
 Norfolk, VA, USA
 dwadduwa@odu.edu

*Corresponding author

Dineth Jayakody
 Old Dominion University
 Norfolk, VA, USA
 dineth.jayakody@cs.odu.edu

Leonidas Zimianitis
 Old Dominion University
 Norfolk, VA, USA
 lzimi001@odu.edu

Abstract

Machine learning (ML) models show strong promise for new biomedical prediction tasks, but concerns about trustworthiness have hindered their clinical adoption. In particular, it is often unclear whether a model relies on true clinical cues or on spurious hierarchical correlations in the data. This paper introduces a simple yet broadly applicable trustworthiness test grounded in stochastic proof-by-contradiction. Instead of just showing high test performance, our approach trains and tests on spurious labels carefully permuted based on a potential outcomes framework. A truly trustworthy model should fail under such label permutation; comparable accuracy across real and permuted labels indicates overfitting, shortcut learning, or data leakage. Our approach quantifies this behavior through interpretable Fisher-style p -values, which are well understood by domain experts across medical and life sciences. We evaluate our approach on multiple new bacterial diagnostics to separate tasks and models learning genuine causal relationships from those driven by dataset artifacts or statistical coincidences. Our work establishes a foundation to build rigor and trust between ML and life-science research communities, moving ML models one step closer to clinical adoption.

1. Introduction

Machine learning approaches have revolutionized multiple facets of biomedical and clinical prediction models. However, the generalizability of some ML-based prediction models remains questionable. Chekroud et al. [5] recently systematically demonstrated that a model trained on data from one clinical study did not generalize to data from other similar studies, in multiple cases. Currently, such failure modes cannot be detected until multiple datasets from multiple studies become available. A high-performing pre-

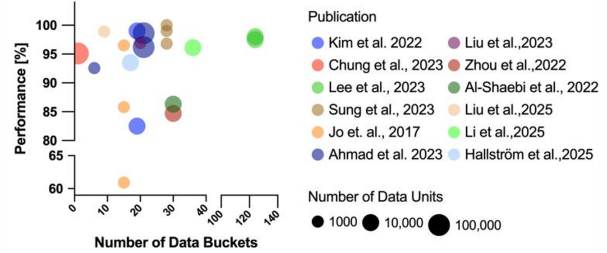


Figure 1. Representative papers with highly accurate deep learning models trained with small numbers of data buckets [1, 2, 6, 14, 19, 21, 23–26, 31, 36, 41]

dition model may mislead researchers to invest millions of dollars of resources in a seemingly promising research direction that may later fail. Thus, a scientifically rigorous technique to evaluate generalizability early on is needed.

Models lack generalizability when they overfit to the training data. Overfitting can be readily detected through well-established “train-validate-test” guidelines with enough independent and identically distributed (IID) data. But when the IID assumption is violated, generalizability conclusions from the standard train-validate-test method are questionable. In general, the IID assumption is related to the data generation (or sampling) process; for scientific and medical data, a domain expert should decide if the data is IID enough before an ML model is utilized, so that the violation can be addressed during model training. However, this critical step is notoriously difficult to practice, and the IID condition is often simply assumed.

We identified a common hierarchy in biomedical data that structurally violates the IID assumption. Large biomedical and clinical datasets often originate from only a few subjects. For example, in a mouse study, millions of cells (data units) can be measured, but they often originate from tens of mice (data buckets). In a pathogen study, mil-

lions of bacteria can be measured, but they often originate from tens of clinical isolates or strains. Similarly, in a clinical trial, thousands of data units may be collected, but they often originate from tens of patients. In all such situations, data units from the same data bucket may very well be correlated, violating the IID assumption. Many biomedical datasets seem to have been curated and used without accounting for this IID violation. For instance, researchers in quantitative phase microscopy (QPM) and Raman spectroscopy, which are two emerging label-free techniques with a broad range of biomedical and clinical applications [33], frequently use ML prediction models. But in many cases, their training datasets are collected from tens of independent specimens. Fig. 1 shows a set of published Phase microscopy [1, 6, 14, 19, 21, 23, 24, 31, 36] and Raman spectroscopy [2, 25, 26, 41] studies that used thousands to hundreds of thousands of data units to train ML models with impressive near-100% accuracy. But these data units originated from a much fewer data buckets (see the x-axis in Fig. 1). Our results (in Section 4) suggest that some of these models likely suffer from non-IID sampling and may not be trustworthy.

This paper proposes a simple yet broadly applicable test to evaluate model generalizability in the presence of possible hierarchical non-IID data. Our method is grounded on the Rubin causal model (RCM) [16] (also known as the potential outcomes framework). Instead of just showing superior test performance, our approach trains and tests on spurious labels carefully permuted by RCM, based on the data hierarchy. If the models trained on spurious labels perform as well as the original, the original model is unreliable despite high accuracy. As a metric of trustworthiness, our approach calculates Fisher-style p-values [4], which are well understood by domain experts across medical and life sciences. Thus, our contributions will lay the very foundation to build rigor and trust between ML and life-science research communities.

Our main contributions are as follows:

- We systematically identify and formalize a pervasive non-IID sampling structure in biomedical datasets, termed the many-units-few-buckets phenomenon, which challenges the validity of conventional train-validate-test evaluation pipelines.
- We propose a framework grounded in the Rubin causal model that quantifies model trustworthiness through a permutation-based stochastic proof-by-contradiction, offering a principled statistical test for trustworthiness.
- We introduce a universal, interpretable, and dataset-agnostic benchmark for evaluating ML reliability across diverse biomedical imaging domains, providing a standardized measure of trustworthiness beyond conventional accuracy metrics.

2. Related Work

Many biomedical ML applications report excellent internal performance, yet audits show these scores often overstate *trustworthy* generalization. One concern is hidden violations of independence in evaluation. Tampu et al. [37] show that splitting volumetric OCT scans at the per-image level induces train-test leakage because adjacent B-scans from the same volume are near-duplicates, inflating accuracy by up to 30% versus subject/volume-level splits. Kapoor and Narayanan [20] review ML applications and document 294 papers with data leakage, including duplicate or near-duplicate samples across splits and temporal or sampling biases that misalign evaluation and target populations. These works suggest that standard train-validate-test pipelines under unexamined IID assumptions can mislead about reliability.

A second line of work traces these failures to *shortcut learning*, where models exploit cues that correlate with labels only in a narrow regime but are semantically misaligned. Geirhos et al. [11] argue that deep networks follow a “path of least resistance,” e.g., textures or context rather than object shape, and thus generalize poorly under distribution shifts. In chest radiography, Zech et al. [39] show pneumonia detectors trained on one hospital’s X-rays achieve strong internal AUC but degrade on external hospitals because they learn hospital-specific signatures instead of pathology. Similarly, DeGrave et al. [9] find radiographic COVID-19 detectors with near-perfect internal AUC rely on laterality markers, projection type, or institution-specific processing instead of genuine pathology. Explanatory analyses such as Lapuschkin et al. [22] uncover similar “Clever Hans” behavior, where high test accuracy is driven by dataset artifacts rather than the intended signal. Together, these studies show that high i.i.d. accuracy alone is insufficient to guarantee clinically meaningful behavior, especially when data exhibit strong, but often unmodeled, hierarchical structure across buckets such as sites, patients, or specimens.

Several works define richer notions of *trustworthiness* for biomedical ML. In medical imaging, the consensus statement by Aldieri et al. [3] conceptualizes the *credibility* of ML predictors as knowing prediction error across a specified information space and advocates a seven-step assessment covering context of use, uncertainty quantification, error decomposition, and robustness to biases. At the prediction level, Nicora et al. [30] review methods for assessing the reliability of predictions and introduce a classifier-agnostic framework combining a *density principle* (flagging inputs far from the training distribution) with a *local fit principle* (checking whether the model was accurate on nearby training points), enabling selective rejection of unreliable cases. Socio-technical work by Zicari et al. [42] introduces the Z-Inspection® process to assess a deployed OHCA de-

tection system, surfacing issues around alert fatigue, fairness, accountability, and continuous monitoring. While these frameworks move beyond raw accuracy, they require problem-specific analyses or system-level auditing and do not offer a *universal statistical test* for arbitrary biomedical classifiers to check whether reported performance is compatible with genuine learning under hierarchical data generation.

Causal inference offers a principled lens on robustness and interpretability in ML, including under non-IID sampling. Surveys such as Guo et al. [13] and Jiao et al. [17] review how structural causal models and potential-outcomes frameworks guide effect estimation and causal discovery across data regimes with interference, networks, and temporal dependence. In healthcare, Sanchez et al. [34] argue that embedding causal structure into clinical ML and precision medicine can mitigate shortcut learning and improve out-of-distribution performance. Closer to our setting, Zhang et al. [40] analyze causal estimation under non-IID sampling induced by interference between units with partially known interaction graphs; they quantify bias from naively assuming IID, propose subset-selection-based debiasing, and characterize identifiability of a “true” causal effect.

Non-IID structure also arises in federated learning (FL), where sites or devices act as natural buckets. Shae et al. [35] argue that the “more data is better” intuition can fail in healthcare FL because cross-hospital datasets are typically non-IID, and propose metrics and clustering strategies to quantify and accommodate inter-site skews. Jimenez-Gutierrez et al. [18] empirically quantify non-IIDness via Hellinger distance across label, feature, quantity, and spatiotemporal skews, showing how these skews degrade FL accuracy and recommending routinely reporting non-IID metrics. These works make non-independence explicit at the level of networks or sites and provide tools for learning with complex sampling, but they largely assume the hierarchy is known and target model design and aggregation rather than a general-purpose hypothesis test for the trustworthiness of a given trained classifier.

Our work also connects to classifier-based hypothesis testing and permutation-based inference. The Classifier Two-Sample Test (C2ST) of Friedman [10] reframes distribution comparison as binary classification and uses hold-out accuracy as a test statistic to detect differences between two i.i.d. samples. Permutation tests for classifier performance [32] estimate empirical p -values by comparing observed error to a null distribution obtained by permuting labels (or features) under IID sampling. Extending such ideas, Mi et al. [28] propose PermFIT, a model-agnostic feature-importance test that uses permutation-based error increases and cross-fitting to obtain per-feature p -values without refitting the base learner. In positive–unlabeled learning, Xu

and Ackerman [38] couple PU-bagging with a permutation test over P/U labels to decide whether predictions meaningfully generalize to unlabeled data. These approaches bring nonparametric hypothesis testing closer to modern ML but generally assume IID samples and treat permutations at the individual-example or feature level rather than respecting a hierarchical data-generation process.

In contrast to prior work, we make the *hierarchy of biomedical data generation* explicit and use it as the backbone of our evaluation procedure. Many biomedical studies collect thousands to millions of data units (cells, spectra, image patches) from only tens to hundreds of buckets (patients, specimens, sites, time points), but this many-units–few-buckets structure is rarely formalized in ML evaluations. Building on the potential-outcomes framework and classifier-based tests such as C2ST, we construct a Rubin-style causal null in which bucket-level labels are stochastically permuted and test whether a model’s observed accuracy can be explained by this null. If a model continues to perform well under bucket-level label permutations, its apparent success can be attributed to hierarchical or other non-IID artifacts rather than genuine learning of label-relevant features. Quantifying evidence against this null through Fisher-style permutation p -values yields a universal, model- and dataset-agnostic notion of *causal significance* that complements existing trustworthiness frameworks, causal ML methods, and permutation-based tests and directly targets the many-units–few-buckets phenomenon pervasive in biomedical imaging.

3. Methodology

Before we introduce the formalism, we illustrate our main idea through an example. Consider a new ML-based diagnostic for antimicrobial resistance (AMR). As shown in Fig. 2, we may image bacteria from a group of resistant samples and compare their images to those from an antimicrobial-susceptible group of samples. Note that each sample contains many bacteria with the same label (either resistant or susceptible). Thus, even with a few samples (data buckets), one can generate many individual data points (data units) to train an ML classifier. Typically, if the trained model accurately predicts resistant vs. susceptible on the test data, we would trust the model. Yet this conclusion is only valid if the data within the buckets aren’t correlated due to reasons other than AMR.

In our proposed framework, rather than simply trusting the test accuracy, we treat the classification process as a hypothesis test, with our test accuracy as the test statistic. Our preferred hypothesis is that the bacterial images contain an underlying signature of AMR that can be detected by a machine learning classifier. The corresponding null hypothesis asserts the absence of such a signature, meaning the class labels contain no information. Under the null hypoth-

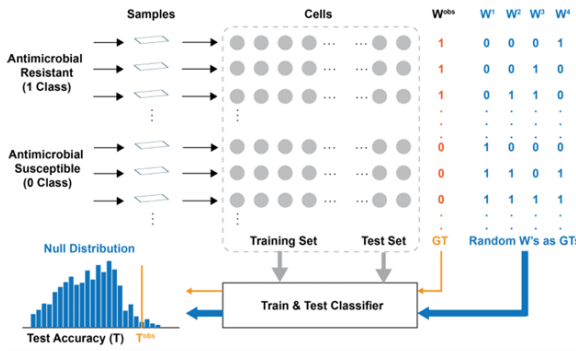


Figure 2. Overview of the proposed causal null-model framework for evaluating model trustworthiness through permutation-based stochastic proof-by-contradiction. Observed bucket-level labels \mathbf{W}^{obs} serve as ground truth (GT). Random permutations $\{\mathbf{W}^{(m)}\}_{m=1}^M$ act as alternative ground truths to form the null distribution of test accuracies. The Fisher-style p -value quantifies whether the observed model performance T_{obs} is significantly higher than those obtained under random label assignments.

esis, if we randomly permute the bucket-level class labels (denoted as permutations $\{W_1, W_2, W_3, \dots\}$ in Fig. 2) and train a classifier on each permuted dataset, those classifiers should perform similarly to the original classifier trained on the true labels. Repeating this experiment across many random permutations allows us to generate a histogram of accuracy values that approximate the null distribution of the test statistic. The Fisher-style p -value, computed as the percentile rank of the observed classifier’s performance, T_{obs} , quantifies the evidence against the null hypothesis. Higher p -values indicate that the null hypothesis of no signature cannot be rejected irrespective of the performance of the original classifier.

Next, we formalize our approach and review essential statistical tools for causal inference and permutation testing.

3.1. Classification with Bucket-Structured Data

Let $\mathcal{D} = \{(\mathbf{x}_i, y_i)\}_{i=1}^N$ be a labeled dataset, where $\mathbf{x}_i \in \mathcal{X}$ (e.g., an image or spectrum) and $y_i \in \mathcal{Y} = \{1, \dots, K\}$ is a class label ($K \geq 2$). The data are grouped into B independent biological *buckets* (e.g., patients, mice, or isolates):

$$\mathcal{D} = \bigcup_{b=1}^B \mathcal{D}_b, \quad \mathcal{D}_b = \{(\mathbf{x}_i, y_i) : i \in \mathcal{I}_b\}, \quad (1)$$

where \mathcal{I}_b denotes the *index set* of samples belonging to bucket b , such that each $\mathcal{I}_b \subseteq [N] = \{1, 2, \dots, N\}$. With $\mathcal{I}_b \cap \mathcal{I}_{b'} = \emptyset$ and $\bigcup_b \mathcal{I}_b = [N]$, all units within a bucket share the same class label: $y_i = W_{b(i)}$, where $b(i)$ maps unit i to its bucket and $W_b \in \mathcal{Y}$ is the bucket-level label. This hierarchical structure induces intra-bucket correlation,

violating the IID assumption and leading to inflated accuracy in standard train-validate-test splits.

A classifier $f_\theta : \mathcal{X} \rightarrow \mathcal{Y}$ is trained to minimize the empirical risk on a training partition. Performance on a test set \mathcal{S} is evaluated using a chosen test statistic $T(\mathcal{S})$, such as accuracy:

$$T(\mathcal{S}) = \text{Acc}(f_\theta, \mathcal{S}) = \frac{1}{|\mathcal{S}|} \sum_{(\mathbf{x}, y) \in \mathcal{S}} \mathbb{I}[f_\theta(\mathbf{x}) = y]. \quad (2)$$

Although accuracy is sensitive to class imbalance, this does not invalidate the permutation test because the null distribution is generated under the same imbalanced data structure. The test remains valid for detecting whether the model exploits systematic bucket-level signal beyond chance, even if raw accuracy is inflated.

3.2. Causal Null Hypothesis via the Rubin Model

Following the Rubin causal model, we treat the bucket label W_b as a treatment assignment applied to all units in bucket b . The causal null hypothesis (H_0) states that, conditional on bucket identity, the features contain no class-specific predictive signal:

$$H_0 : \mathbf{x}_i \perp\!\!\!\perp W_{b(i)} \mid b(i). \quad (3)$$

where $\perp\!\!\!\perp$ denotes statistical independence and $b(i)$ maps each sample to its corresponding bucket. Under H_0 , reassigning bucket labels should not increase accuracy beyond chance.

3.3. Permutation Test

To test H_0 , we perform bucket-level label permutation. Let $\mathbf{W}^{\text{obs}} = (W_1, \dots, W_B)$ be the observed bucket labels. A random permutation $\pi : [B] \rightarrow [B]$ generates:

$$\mathbf{W}^{(\pi)} = (W_{\pi(1)}, \dots, W_{\pi(B)}), \quad y_i^{(\pi)} = W_{\pi(b(i))}. \quad (4)$$

The permuted dataset is $\mathcal{D}^{(\pi)} = \{(\mathbf{x}_i, y_i^{(\pi)})\}_{i=1}^N$. Under H_0 , the distribution of accuracy $T(\mathcal{D}^{(\pi)})$ is exchangeable across all permutations π .

Under the alternative hypothesis (H_1), the features \mathbf{x}_i carry genuine class-specific signal, such that the observed accuracy $T_{\text{obs}} = T(\mathcal{D})$ is expected to be significantly higher than those obtained under random label permutations. Rejecting H_0 in favor of H_1 thus indicates that the classifier has captured a true, generalizable relationship between the features and the bucket-level labels.

3.4. Fisher-Style p -Value via Permutation Testing

To quantify statistical significance, we use Fisher’s exact randomization principle. Under the null hypothesis H_0 , permuting the bucket-level labels does not affect the test statistic. Let Π_B denote the set of all possible label permutations

across B buckets. For each permutation $\pi \in \Pi_B$, we train a classifier on the permuted dataset $\mathcal{D}^{(\pi)}$ and compute its test statistic:

$$T_\pi = T(\mathcal{D}^{(\pi)}). \quad (5)$$

The observed statistic on the true labels is $T_{\text{obs}} = T(\mathcal{D})$. The Fisher-style p -value is defined as:

$$p = \frac{\sum_{\pi \in \Pi_B} \mathbb{I}[T_\pi \geq T_{\text{obs}}]}{|\Pi_B|}. \quad (6)$$

where $\mathbb{I}[\cdot]$ is the indicator function that equals 1 if the condition inside the brackets is true and 0 otherwise. This measures the probability, under random bucket-level label assignments, of obtaining a test statistic at least as large as the observed one. A small p -value (e.g., $p < 0.05$) rejects H_0 , indicating that the classifier's performance cannot be explained by chance and thus reflects a generalizable signal. In practice, since the number of unique label permutations $M = |\Pi_B|$ is finite, the p -value is discrete, and its minimum attainable value is $p_{\min} = 1/M$. This lower bound determines the resolution of statistical significance, that results with p approaching p_{\min} indicate the strongest possible evidence against H_0 given the available number of permutations.

4. Evaluation

We evaluate our proposed framework on both controlled benchmarks and published biomedical datasets. The toy benchmarks validate the framework's expected behavior based on a simulated visual cue (and the lack thereof), while the biomedical experiments demonstrate its utility for evaluating trustworthiness in real-world scenarios.

4.1. Controlled Benchmarks

We design controlled benchmarks in which the strength of the underlying causal signal can be explicitly manipulated. We consider two datasets, Rotated MNIST and Colored FashionMNIST, each constructed to introduce visual cues under well-defined conditions. Across all experiments, we employ two representative architectures: a lightweight convolutional neural network (*LightCNN*) and a compact Vision Transformer (*LightViT*). The *LightCNN* serves as a strong inductive baseline that captures local spatial structure, while the *LightViT* provides an attention-based counterpart capable of modeling global dependencies. Both models are used consistently across all experiments to establish controlled and reproducible benchmarks for evaluating the proposed framework (model details described in Supplementary Section).

4.1.1. Rotated MNIST

We evaluate whether a rotation cue enables binary discrimination on the MNIST dataset. Digits $\{0, 1, 2, 3, 4\}$

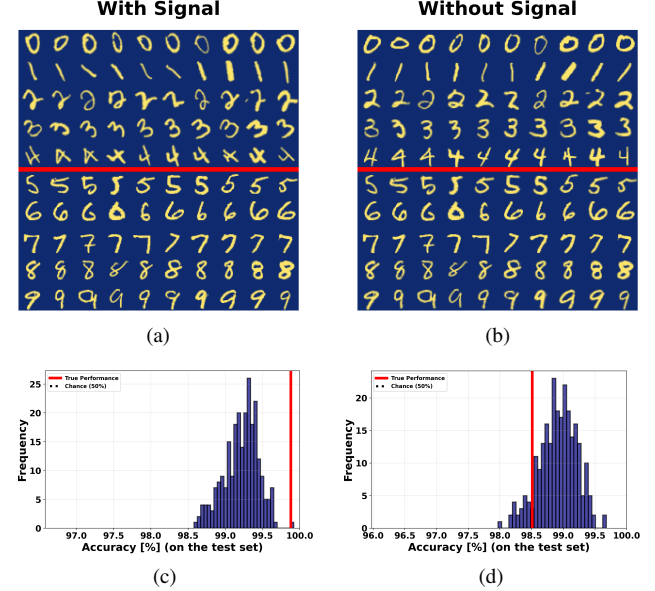


Figure 3. Simulated MNIST example with and without a causal signal on LightCNN. (a) Digits rotated by 45° introduce a treatment cue, yielding significant separation between observed and null accuracies. (b) Without rotation, no true signal exists despite high apparent accuracy.

are defined as *treated* (T) and digits $\{5, 6, 7, 8, 9\}$ as *untreated* (F). For each experiment, a per-class rotation angle is sampled from truncated Gaussian distributions ($T \sim \mathcal{N}(\theta, \sigma = 2^\circ)$, $F \sim \mathcal{N}(0^\circ, \sigma = 2^\circ)$), clipped to the interval $[-90^\circ, 90^\circ]$. Each image of a given class is rotated by its corresponding class angle using bilinear interpolation (no expansion, fill value = 0). We sweep treatment angles $\theta \in \{0^\circ : 5^\circ : 30^\circ\} \cup \{45^\circ, 60^\circ, 90^\circ\}$, using a unique random seed for angle generation and a fixed seed for deterministic training. We perform a permutation test for all unique class-to-label assignments. For each permutation, the models were trained for 5 epochs to produce a null accuracy distribution, from which the p -value is computed.

As shown in Fig. 3, when no signal was introduced (0° rotation), the *LightCNN* still achieved a high apparent accuracy ($\sim 99\%$) but with a high p -value ($p = 0.9685$), demonstrating that accuracy alone can be misleading as a measure to trust the model detecting an expected cue. In contrast, when 45° rotation was applied, the p -value dropped close to the theoretical minimum ($p = 0.0080$) along with a slight increase in the model accuracy. Results for additional rotation angles are summarized in Table 1, showing the same trend as the causal signal strength increases.

Surprisingly, *LightViT*'s p -value remained high despite the strength of the causal cue, suggesting a reliance on bucket-level structure over the simulated rotation. Prior Rotated MNIST studies—e.g., Ghifary et al. [12] and Motiian

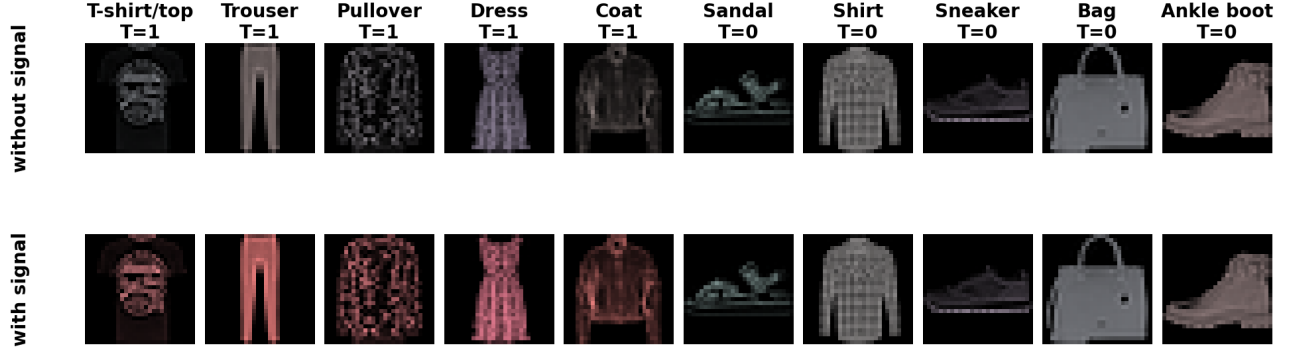


Figure 4. Sample images Top: RGB versions of the images without any class-dependent color manipulation; Bottom: RGB images with class-dependent red scaling and shared green/blue baselines, altering global color without changing spatial structure.

et al. [29]—although in a different setting, also report unusually low performance specifically at 45° due to increased class overlap. Consistent with this, we observe that particularly at 45° rotation, *LightViT* behaves unexpectedly with $p = 0.3360$. These results indicate that *LightViT* is not well-aligned with the rotational cue under study. More broadly, the observed p -values suggest that permutation-based significance testing may help identify whether a given model is suitable for a target causal cue. A deeper investigation of these effects is left for future work.

4.1.2. Colored FashionMNIST

We test whether a color cue enable binary discrimination on FashionMNIST. Classes $\{\text{T-shirt/Top, Trouser, Pullover, Dress, Coat}\}$ are defined as *treated* ($T=1$), and $\{\text{Sandal, Shirt, Sneaker, Bag, Ankle Boot}\}$ as *untreated* ($T=0$). Each grayscale image $\mathbf{I} \in [0, 1]^{H \times W}$ is first replicated across RGB channels. Per-image channel multipliers are sampled from normal distributions:

$$\text{If } T=1 : \quad r \sim \mathcal{N}(\mu_R, \sigma_R^2), \quad (7)$$

$$g, b \sim \mathcal{N}(\mu_F, \sigma_F^2); \quad (8)$$

$$\text{If } T=0 : \quad r, g, b \sim \mathcal{N}(\mu_F, \sigma_F^2) \text{ independently.} \quad (9)$$

The colorized image is generated by scaling the grayscale input:

$$(\mathbf{R}', \mathbf{G}', \mathbf{B}') = \text{clip}(\mathbf{I} \odot (r, g, b), 0, 1), \quad (10)$$

where \odot denotes elementwise multiplication. Here, $\mu_F = 0.5$ and $\sigma_F = 0.03$ are shared across the green and blue channels in both groups, while treatment strength is controlled by varying μ_R over multiple levels ($\mu_R \in [0.55, 0.85]$, $\Delta = 0.05$). This process alters only the global red color intensity (which is the signal) per image, preserving spatial structure (refer Fig. 4).

For each treatment level we perform all unique permutations, where each permutation retrains the models

Table 1. Evaluation on controlled benchmarks using LightCNN and LightViT architectures. Observed accuracy is computed under true label assignments, and lower p -values indicate stronger causal evidence. Here, $p_{\min} = 0.0040$ for both experiments.

Dataset	Treatment	LightCNN		LightViT	
		Acc. (%)	p -value	Acc. (%)	p -value
Rotated MNIST	0°	98.51	0.9080	95.59	0.5360
	5°	98.88	0.7280	96.55	0.2960
	10°	99.70	0.0080	96.89	0.2360
	15°	99.73	0.0080	93.33	0.8560
	20°	99.71	0.0080	95.75	0.6040
	25°	99.73	0.0080	97.46	0.1400
	30°	99.82	0.0040	98.49	0.0040
	45°	99.88	0.0080	97.23	0.3360
	60°	99.96	0.0040	96.17	0.0880
	90°	99.86	0.0080	98.84	0.0120
Colored FMNIST	$\mu_R = 0.50$	93.66	0.4120	92.28	0.2440
	$\mu_R = 0.55$	94.92	0.1560	94.31	0.0840
	$\mu_R = 0.60$	97.52	0.0240	97.43	0.0120
	$\mu_R = 0.65$	99.16	0.0120	99.02	0.0080
	$\mu_R = 0.70$	99.80	0.0080	99.75	0.0120
	$\mu_R = 0.75$	99.96	0.0080	100.0	0.0040
	$\mu_R = 0.80$	100.0	0.0080	100.0	0.0080
	$\mu_R = 0.85$	100.0	0.0040	100.0	0.0080

for 5 epochs to estimate the null accuracy distribution. As expected, when $\mu_R = 0.5$ —no significant signal is present—the accuracy remains high on both models, but the p -value is also high, indicating no meaningful causal effect. As μ_R increases, accuracy exhibits an upward trend while the p -value decreases, suggesting stronger causal evidence (Table 1). Interestingly, *LightViT* demonstrated same behavior as *LightCNN* suggesting both architectures are trustworthy for the task.

4.2. Real Biomedical Demonstrations

4.2.1. Bacteria Quantitative Phase Microscopy Dataset (QPM-WGS-AMR-21)

We utilize the QPM-WGS-AMR-21 [1] dataset, which contains quantitative phase microscopy (QPM) images of 21 bacterial strains spanning five species: *Acinetobacter baumannii*

Table 2. Evaluation of ResNet-18 on three binary classification tasks. Reported values show single-test accuracy and permutation-based p -values. Minimum attainable resolutions: WT vs NWT ($p_{\min} = 0.0040$), GP vs GN ($p_{\min} = 0.0083$), AB vs KP ($p_{\min} = 0.0080$).

Experiment	Acc. (%)	p -value
WT vs NWT	72.00	0.3120
GP vs GN	76.09	0.3403
AB vs KP	77.04	0.0480

mannii, *Escherichia coli*, *Klebsiella pneumoniae*, *Staphylococcus aureus*, and *Bacillus subtilis*. Each isolate is accompanied by whole genome sequencing (WGS) and antimicrobial resistance (AMR) profiles, enabling tasks such as Gram typing, AMR prediction, species classification, and strain discrimination. We evaluate three binary tasks constructed from this dataset. For AMR prediction (WT vs. NWT), we use ten isolates (five WT, five NWT) following the grouping in Ahmad et al. [1]. The same ten isolates are used for Gram classification (GP vs. GN), comprising three Gram-positive and seven Gram-negative strains. Finally, we include a species-level task distinguishing *Acinetobacter baumannii* (AB) from *Klebsiella pneumoniae* (KP), using nine isolates (four AB, five KP) to provide a complementary pathogen-level benchmark.

For all tasks, we extract embeddings using a pretrained ResNet-18 backbone and train a lightweight classification head, following the setup in prior work [1]. Class-balanced loss weighting is applied where appropriate. As shown in Table 2, ResNet-18 achieves moderate –yet well above random chance– accuracy on WT vs. NWT and GP vs. GN, but the high p -values indicate that these results are not trustworthy under our framework. This suggests that the model does not capture a strong or stable underlying signal for AMR or Gram-level discrimination. In contrast, the AB vs. KP task yields a lower p -value than the other two tasks, indicating a more reliable species-level signal; however, the value remains comparatively large relative to its own p_{\min} (i.e. $1/M$ where M is the number of permutations), meaning the evidence is still weak.

Overall, these results show that accuracy alone can be misleading. Significance testing using our framework provides an added layer of caution against spurious dataset-driven correlations.

4.2.2. Raman Bacteria-ID Dataset

Raman spectroscopy is an emerging label-free technique increasingly used for biomedical applications, including pathogen detection. Here we use the public Raman bacteria-ID dataset from Ho et al. [15], which contains Raman spectra of 30 bacterial and yeast isolates acquired with a 633 nm laser on gold-coated silica substrates. Each isolate provides

Table 3. Causal evaluation for Penicillin vs. Meropenem and MRSA vs. MSSA. Lower p -values indicate stronger causal significance. (Here, $p_{\min} = 0.0002$ for Penicillin vs. Meropenem and $p_{\min} = 0.1000$ for MRSA vs. MSSA.)

Model	Penicillin vs. Meropenem		MRSA vs. MSSA	
	Acc. (%)	p	Acc. (%)	p
Simple MLP	75.00	0.1050	80.20	0.8000
Improved MLP	77.80	0.0010	73.80	1.0000
RamanNet [41]	80.14	0.0150	70.40	0.9000

~2,000 low-signal-to-noise spectra, along with two clinical cohorts containing 400 and 100 spectra per isolate. Labels include species identity, empiric antibiotic group, and binary resistance status for methicillin-resistant *Staphylococcus aureus* (MRSA) as methicillin-susceptible *S. aureus* (MSSA), making this a large-scale benchmark for Raman-based bacterial classification [2, 25, 26, 41].

We evaluate two binary tasks from this dataset: (i) Penicillin vs. Meropenem antibiotic grouping, and (ii) MRSA vs. MSSA resistance classification. The Penicillin vs. Meropenem task is challenging because each antibiotic group contains multiple isolates with highly similar Raman spectra, creating a high risk of overfitting to strain-level artifacts. We first trained a three-layer MLP baseline using 1000-dimensional Raman inputs. As shown in Table 3, this model achieved reasonable accuracy but yielded high p -values, indicating weak trustworthiness in our framework. We then evaluated an improved MLP with spectral derivatives, residual connections, LayerNorm, and GELU, along with the RamanNet architecture [41] (more model details in the supplementary). Both models produced higher accuracies and much lower p -values, demonstrating that the underlying antibiotic-group signal is detectable when a sufficiently expressive model is used. Thus, our framework distinguishes whether a negative result reflects non-IID structure or simply an underpowered model. For the MRSA vs. MSSA task, the Raman spectra for the two classes are nearly indistinguishable (Fig. 5). Yet all models achieved well-above-chance accuracies (Table 3). But the corresponding p -values remained high across architectures (Table 3), indicating a consensus on the lack of a Raman signal indicative of AMR (related to MRSA/MSSA).

Misclassifying MRSA as MSSA in clinical practice can cause serious treatment failures, such as longer infections, higher mortality (20–50% increase when therapy is delayed), and faster spread of resistance [7, 27]. On the other hand, labeling MSSA as MRSA can lead to unnecessary use of vancomycin, increasing the risk of kidney damage, *C. difficile* infections, and selection for vancomycin-resistant bacteria [8]. Because of these high clinical risks, trustworthiness frameworks like ours are critical to identify when and when not to trust future Raman-based diagno-

tics.

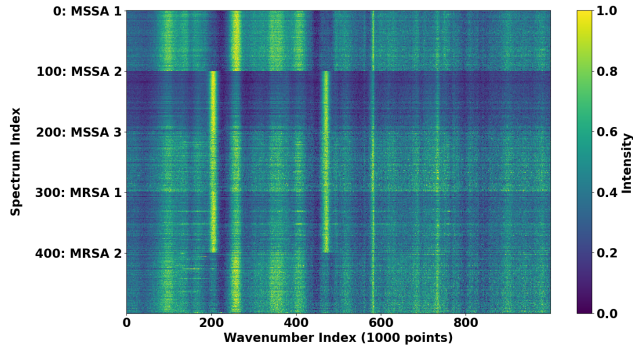


Figure 5. Representative Raman spectra for the MRSA vs. MSSA experiment. Each subclass (MRSA 1–2, MSSA 1–3) contains 100 spectra, with 1000 Raman shift points per spectrum. Spectral profiles between MRSA and MSSA appear visually similar, highlighting the challenge of discriminating antibiotic resistance from spectral data alone.

5. Ablation Study

Training a model for each permutation is computationally expensive. We reduce this cost using ground-truth-free pre-training and by sampling a subset of permutations. We first assess how pretraining impacts convergence and runtime, and then evaluate how many permutations are needed for stable and efficient p -value estimation.

5.1. Effect of Pretraining on Evaluation Efficiency

As shown in Table 4, Masked Autoencoder (MAE)-based pretraining substantially reduces the total computation cost while maintaining comparable causal significance. In the Penicillin vs. Meropenem experiment, MAE pretraining achieved approximately a 40% reduction in total evaluation time compared to training from scratch, with a consistent causal trend ($p = 0.009$). A similar improvement is observed in the WT vs. NWT experiment, where self-supervised pretraining with ResNet-18 led to an estimated 95% decrease in computation time. These results highlight that pretrained feature representations enable faster convergence and efficient permutation testing by eliminating the need for full model retraining, achieving over a 90% overall reduction in evaluation time without compromising interpretability or causal reliability. Future work will further explore additional pretrained methods to enhance robustness and generalizability across diverse datasets.

5.2. Number of Permutations for Stable Causal Inference

The stability of causal inference depends on the number of random label permutations used to approximate the null distribution. Evaluating all permutations guarantees the ex-

Table 4. Comparison of pretrained and non-pretrained models for RamanNet (Penicillin vs. Meropenem) and ResNet-18 (WT vs. NWT). (Here, $p_{\min} = 0.0002$ for Penicillin vs. Meropenem and $p_{\min} = 0.0083$ for WT vs. NWT)

Experiment	Embed. time (min:s)	Perm. time (min:s)	Acc. (%)	p -value
Penicillin vs. Meropenem				
Without Pretraining	–	36 : 23	80.14	0.0160
With MAE Pretraining	0 : 38	22 : 43	73.67	0.0100
WT vs. NWT				
Without Pretraining	–	651 : 55	79.88	0.6059
With MAE Pretraining	12 : 00	11 : 27	72.00	0.3120

act Fisher-style p -value but is computationally expensive; therefore, we analyze how partial sampling behaves.

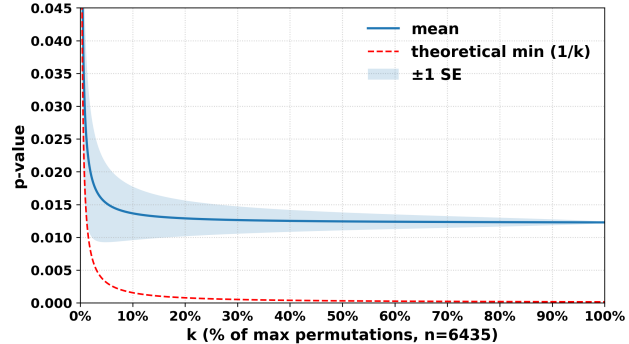


Figure 6. Convergence of causal p -value estimation with increasing number of sampled permutations.

For the Penicililine vs Meropenem task, we found that the estimated causal p -values rapidly converge even when using a small subset of permutations. Although the full null distribution contained 6,435 permutations, stable estimates were achieved with only 1,000 samples, producing p -values within the same significance range as full enumeration. As shown in Fig. 6, p -values stabilize after evaluating only $\sim 15.54\%$ of all permutations, enabling over $\sim 84.46\%$ time savings with no loss of statistical reliability.

6. Conclusion

We present a framework that redefines how trustworthiness in ML should be evaluated. Instead of relying solely on high test accuracy, our stochastic proof-by-contradiction approach provides a causal benchmark, requiring models to fail under data-hierarchy-aware randomized label permutations if they are truly learning meaningful patterns. By integrating data-hierarchy-aware permutations on the Rubin causal model, to calculate Fisher-style p -values, our method establishes a unified, interpretable standard that every ML study (especially bio-medical and clinical ones) can adopt to verify when IID assumptions are questionable. Our results across multiple datasets highlight clear guidelines for future evaluations that causal significance should

accompany accuracy. Our framework thus serves as a reproducible, model-agnostic foundation for reliable and scientifically rigorous ML evaluation.

References

- [1] Azeem Ahmad, Ramith Hettiarachchi, Abdolrahman Khezri, Balpreet Singh Ahluwalia, Dushan N Wadduwage, and Rafi Ahmad. Highly sensitive quantitative phase microscopy and deep learning aided with whole genome sequencing for rapid detection of infection and antimicrobial resistance. *Frontiers in Microbiology*, 14:1154620, 2023. [1](#), [2](#), [6](#), [7](#)
- [2] Zakarya Al-Shaebi, Fatma Uysal Ciloglu, Mohammed Nasser, and Omer Aydin. Highly accurate identification of bacteria's antibiotic resistance based on raman spectroscopy and u-net deep learning algorithms. *ACS omega*, 7(33):29443–29451, 2022. [1](#), [2](#), [7](#)
- [3] Alessandra Aldieri, Thiranja Prasad Babarenda Gamage, Antonino Amedeo La Mattina, Axel Loewe, Francesco Papalardo, and Marco Viceconti. Consensus statement on the credibility assessment of machine learning predictors. *Briefings in Bioinformatics*, 26(2):bbaf100, 2025. [2](#)
- [4] M-AC Bind and DB Rubin. When possible, report a fisher-exact p value and display its underlying null randomization distribution. *Proceedings of the National Academy of Sciences*, 117(32):19151–19158, 2020. [2](#)
- [5] Adam M Chekroud, Matt Hawrilenko, Hieronimus Loho, Julia Bondar, Ralitsa Gueorguieva, Alkomiet Hasan, Joseph Kambeitz, Philip R Corlett, Nikolaos Koutsouleris, Harlan M Krumholz, et al. Illusory generalizability of clinical prediction models. *Science*, 383(6679):164–167, 2024. [1](#)
- [6] Yoonjae Chung, Geon Kim, Ah-Rim Moon, DongHun Ryu, Herve Hugonnet, Mahn Jae Lee, DongSeong Shin, Seung-Jae Lee, Eek-Sung Lee, and YongKeun Park. Label-free histological analysis of retrieved thrombi in acute ischemic stroke using optical diffraction tomography and deep learning. *Journal of Biophotonics*, 16(8):e202300067, 2023. [1](#), [2](#)
- [7] Sara E Cosgrove, George Sakoulas, Eli N Perencevich, Mitchell J Schwaber, Adolf W Karchmer, and Yehuda Carmeli. Comparison of mortality associated with methicillin-resistant and methicillin-susceptible staphylococcus aureus bacteremia: a meta-analysis. *Clinical infectious diseases*, 36(1):53–59, 2003. [7](#)
- [8] Stephanie J Dancer. Importance of the environment in methicillin-resistant staphylococcus aureus acquisition: the case for hospital cleaning. *The Lancet infectious diseases*, 8(2):101–113, 2008. [7](#)
- [9] AJ DeGrave, JD Janizek, and SI Lee. Ai for radiographic covid-19 detection selects shortcuts over signal. *nat. mach. intell.* 3, 610–619, 2021. [2](#)
- [10] Jerome Friedman. On multivariate goodness-of-fit and two-sample testing. Technical report, SLAC National Accelerator Laboratory (SLAC), Menlo Park, CA (United States), 2004. [3](#)
- [11] Robert Geirhos, Jörn-Henrik Jacobsen, Claudio Michaelis, Richard Zemel, Wieland Brendel, Matthias Bethge, and Felix A Wichmann. Shortcut learning in deep neural networks. *Nature Machine Intelligence*, 2(11):665–673, 2020. [2](#)
- [12] Muhammad Ghifary, W Bastiaan Kleijn, Mengjie Zhang, and David Balduzzi. Domain generalization for object recognition with multi-task autoencoders. In *Proceedings of the IEEE international conference on computer vision*, pages 2551–2559, 2015. [5](#)
- [13] Ruocheng Guo, Lu Cheng, Jundong Li, P Richard Hahn, and Huan Liu. A survey of learning causality with data: Problems and methods. *ACM Computing Surveys (CSUR)*, 53(4):1–37, 2020. [3](#)
- [14] Erik Hallström, Vinodh Kandavalli, Carolina Wählby, and Anders Hast. Rapid label-free identification of seven bacterial species using microfluidics, single-cell time-lapse phase-contrast microscopy, and deep learning-based image and video classification. *Plos one*, 20(9):e0330265, 2025. [1](#), [2](#)
- [15] Chi-Sing Ho, Neal Jean, Catherine A Hogan, Lena Blackmon, Stefanie S Jeffrey, Mark Holodniy, Niaz Banaei, Amr AE Saleh, Stefano Ermon, and Jennifer Dionne. Rapid identification of pathogenic bacteria using raman spectroscopy and deep learning. *Nature communications*, 10(1):4927, 2019. [7](#)
- [16] Guido W Imbens and Donald B Rubin. Rubin causal model. In *The new palgrave dictionary of economics*, pages 1–10. Springer, 2008. [2](#)
- [17] Licheng Jiao, Yuhang Wang, Xu Liu, Lingling Li, Fang Liu, Wenping Ma, Yuwei Guo, Puhua Chen, Shuyuan Yang, and Biao Hou. Causal inference meets deep learning: A comprehensive survey. *Research*, 7:0467, 2024. [3](#)
- [18] Daniel M Jimenez-Gutierrez, Mehrdad Hassanzadeh, Aris Anagnostopoulos, Ioannis Chatzigiannakis, and Andrea Vittalenti. A thorough assessment of the non-iid data impact in federated learning. *arXiv preprint arXiv:2503.17070*, 2025. [3](#)
- [19] YoungJu Jo, Sangjin Park, JaeHwang Jung, Jonghee Yoon, Hosung Joo, Min-hyeok Kim, Suk-Jo Kang, Myung Chul Choi, Sang Yup Lee, and YongKeun Park. Holographic deep learning for rapid optical screening of anthrax spores. *Science advances*, 3(8):e1700606, 2017. [1](#), [2](#)
- [20] Sayash Kapoor and Arvind Narayanan. Leakage and the reproducibility crisis in machine-learning-based science. *Patterns*, 4(9), 2023. [2](#)
- [21] Geon Kim, Daewoong Ahn, Minhee Kang, Jinho Park, DongHun Ryu, YoungJu Jo, Jinyeop Song, Jea Sung Ryu, Gunho Choi, Hyun Jung Chung, et al. Rapid species identification of pathogenic bacteria from a minute quantity exploiting three-dimensional quantitative phase imaging and artificial neural network. *Light: Science & Applications*, 11(1):190, 2022. [1](#), [2](#)
- [22] Sebastian Lapuschkin, Stephan Wäldchen, Alexander Binder, Grégoire Montavon, Wojciech Samek, and Klaus-Robert Müller. Unmasking clever hans predictors and assessing what machines really learn. *Nature communications*, 10(1):1096, 2019. [2](#)
- [23] Young Ki Lee, Dongmin Ryu, Seungwoo Kim, Juyeon Park, Seog Yun Park, Donghun Ryu, Hayoung Lee, Sungbin Lim, Hyun-Seok Min, YongKeun Park, et al. Machine-learning-

based diagnosis of thyroid fine-needle aspiration biopsy synergistically by papanicolaou staining and refractive index distribution. *Scientific Reports*, 13(1):9847, 2023. 1, 2

[24] Ying Li, Jianglei Di, Li Ren, and Jianlin Zhao. Deep-learning-based prediction of living cells mitosis via quantitative phase microscopy. *Chinese Optics Letters*, 19(5):051701, 2021. 2

[25] Bo Liu, Kunxiang Liu, Jide Sun, Lindong Shang, Qingxiang Yang, Xueping Chen, and Bei Li. Classification of pathogenic bacteria by raman spectroscopy combined with variational auto-encoder and deep learning. *Journal of Biophotonics*, 16(4):e202200270, 2023. 2, 7

[26] Yukai Liu, Miaomiao Ji, Xiao Ren, Zhenyong Dong, Tian Wen, Qingyue Dong, Ho-pui Ho, Lunbiao Cui, Yanqing Lu, and Guanghui Wang. Deep learning-assisted rapid bacterial classification based on raman spectroscopy of bacteria lysed by acoustically driven fiber-tip vibration. *Advanced Science*, 12(32):e07724, 2025. 1, 2, 7

[27] Thomas P Lodise, Peggy S McKinnon, Linda Swiderski, and Michael J Rybak. Outcomes analysis of delayed antibiotic treatment for hospital-acquired staphylococcus aureus bacteremia. *Clinical infectious diseases*, 36(11):1418–1423, 2003. 7

[28] Xinlei Mi, Baiming Zou, Fei Zou, and Jianhua Hu. Permutation-based identification of important biomarkers for complex diseases via machine learning models. *Nature communications*, 12(1):3008, 2021. 3

[29] Saeid Motian, Marco Piccirilli, Donald A Adjero, and Gi-anfranco Doretto. Unified deep supervised domain adaptation and generalization. In *Proceedings of the IEEE international conference on computer vision*, pages 5715–5725, 2017. 6

[30] Giovanna Nicora, Miguel Rios, Ameen Abu-Hanna, and Riccardo Bellazzi. Evaluating pointwise reliability of machine learning prediction. *Journal of Biomedical Informatics*, 127:103996, 2022. 2

[31] Noga Nissim, Matan Dudaie, Itay Barnea, and Natan T Shaked. Real-time stain-free classification of cancer cells and blood cells using interferometric phase microscopy and machine learning. *Cytometry Part A*, 99(5):511–523, 2021. 1, 2

[32] Markus Ojala and Gemma C Garriga. Permutation tests for studying classifier performance. *Journal of machine learning research*, 11(6), 2010. 3

[33] Juyeon Park, Bijie Bai, DongHun Ryu, Tairan Liu, Chungha Lee, Yi Luo, Mahn Jae Lee, Luzhe Huang, Jeongwon Shin, Yijie Zhang, et al. Artificial intelligence-enabled quantitative phase imaging methods for life sciences. *Nature Methods*, 20(11):1645–1660, 2023. 2

[34] Pedro Sanchez, Jeremy P Voisey, Tian Xia, Hannah I Watson, Alison Q O’Neil, and Sotirios A Tsaftaris. Causal machine learning for healthcare and precision medicine. *Royal Society Open Science*, 9(8):220638, 2022. 3

[35] Zon-Yin Shae, Kun-Yi Chen, Chi-Yu Chang, Yuan-Yu Tsai, Che-Yi Chou, William I Baskett, Chi-Ren Shyu, and Jeffrey JP Tsai. Thoughts on non-iid data impact in healthcare with federated learning medical blockchain. In *2022 IEEE 4th International Conference on Cognitive Machine Intelligence (CogMI)*, pages 20–26. IEEE, 2022. 3

[36] MinDong Sung, Jong Hyun Kim, Hyun-Seok Min, Sooyoung Jang, JaeSeong Hong, Bo Kyu Choi, JuHye Shin, Kyung Soo Chung, and Yu Rang Park. Three-dimensional label-free morphology of cd8+ t cells as a sepsis biomarker. *Light: Science & Applications*, 12(1):265, 2023. 1, 2

[37] Iulian Emil Tampu, Anders Eklund, and Neda Haj-Hosseini. Inflation of test accuracy due to data leakage in deep learning-based classification of oct images. *Scientific Data*, 9(1):580, 2022. 2

[38] Shiwei Xu and Margaret E Ackerman. Leveraging permutation testing to assess confidence in positive-unlabeled learning applied to high-dimensional biological datasets. *BMC bioinformatics*, 25(1):218, 2024. 3

[39] John R Zech, Marcus A Badgeley, Manway Liu, Anthony B Costa, Joseph J Titano, and Eric Karl Oermann. Variable generalization performance of a deep learning model to detect pneumonia in chest radiographs: a cross-sectional study. *PLoS medicine*, 15(11):e1002683, 2018. 2

[40] Chi Zhang, Karthika Mohan, and Judea Pearl. Causal inference with non-iid data under model uncertainty. *Proceedings of Machine Learning Research vol TBD*, 1:14, 2023. 3

[41] Bo Zhou, Yu-Kai Tong, Ru Zhang, and Anpei Ye. Ramanet: a lightweight convolutional neural network for bacterial identification based on raman spectra. *RSC advances*, 12(40):26463–26469, 2022. 1, 2, 7

[42] Roberto V Zicari, James Brusseau, Stig Nikolaj Blomberg, Helle Collatz Christensen, Megan Coffee, Marianna B Ganapini, Sara Gerke, Thomas Krendl Gilbert, Eleanore Hickman, Elisabeth Hildt, et al. On assessing trustworthy ai in healthcare. machine learning as a supportive tool to recognize cardiac arrest in emergency calls. *Frontiers in Human Dynamics*, 3:673104, 2021. 2

Beyond Perfect Scores: Proof-by-Contradiction for Trustworthy Machine Learning

Supplementary Material

1. Model Architectures Details

This section provides full architectural, training, and implementation details for the models used in the controlled benchmarks described in Sec. 4.1. All experiments were implemented in PyTorch 2.0.1 and executed on NVIDIA RTX 6000 Ada Generation GPUs with CUDA 12.2 using mixed-precision training. Random seeds were fixed for all runs to ensure deterministic reproducibility.

1.1. LightCNN Architecture

Model Overview. The *LightCNN* is a compact convolutional neural network designed for low-resolution RGB inputs (28×28) to provide a strong inductive baseline for local spatial learning. (used in Table 1)

Layer Configuration.

- **Input:** RGB image ($3 \times 28 \times 28$).
- **Conv1:** $3 \rightarrow 32$ filters, kernel size 3×3 , stride 1, padding 1; followed by ReLU and 2×2 MaxPool.
- **Conv2:** $32 \rightarrow 64$ filters, kernel size 3×3 , stride 1, padding 1; followed by ReLU and 2×2 MaxPool.
- **Conv3:** $64 \rightarrow 128$ filters, kernel size 3×3 , stride 1, padding 1; followed by ReLU and 2×2 MaxPool.
- **Flatten:** Output feature map ($128 \times 3 \times 3$) flattened to a 1152-D vector.
- **FC1:** Linear(1152, 256), ReLU, Dropout($p = 0.5$).
- **FC2:** Linear(256, 2) for binary classification.

Training Configuration.

- Optimizer: Adam
- Learning rate: 1×10^{-4}
- Batch size: 64
- Epochs: 5 per permutation
- Loss: CrossEntropyLoss
- Dropout: 0.5

1.2. LightViT Architecture

Model Overview. The *LightViT* is a compact Vision Transformer adapted for 28×28 inputs. It employs a convolutional patch embedding stem to project local patches into a low-dimensional embedding space, followed by a lightweight Transformer encoder for global feature learning. (used in Table 1)

Patch Embedding.

- Patch size: 4×4 , stride 4
- Number of patches: $7 \times 7 = 49$
- Embedding dimension: 96

- Operation: Conv2d($3, 96$, kernel = 4, stride = 4) followed by flattening and transposing to $(B, 49, 96)$

Positional and Classification Tokens.

- Learnable CLS token of shape $(1, 1, 96)$
- Learnable positional embedding $(1, 50, 96)$ (49 patches + 1 CLS)
- Dropout applied to combined embeddings ($p = 0.1$)

Transformer Encoder.

- Number of encoder blocks: 6
- Embedding dimension: 96
- Attention heads: 3
- MLP hidden dimension: 384 (96×4)
- Attention dropout: 0.1
- MLP dropout: 0.1
- Normalization: LayerNorm before attention and MLP
- Activation: GELU

Classifier Head.

- CLS token representation \rightarrow Linear($96, 2$) for binary prediction.

Initialization.

- CLS and positional embeddings: truncated normal ($\sigma = 0.02$)
- Linear and MLP layers: truncated normal ($\sigma = 0.02$), zero bias
- Convolution layers: Kaiming Normal initialization

Training Configuration.

- Optimizer: Adam
- Learning rate: 1×10^{-4}
- Batch size: 64
- Epochs: 5 per experiment or permutation
- Loss: CrossEntropyLoss
- Dropout: 0.1

1.3. Simple MLP Architecture

Model Overview - The *Simple MLP* is a Multi-Layer Perceptron designed for binary classification tasks with high-dimensional input features. It employs a series of fully connected layers with batch normalization and dropout regularization to learn discriminative representations from input feature vectors. (used in Table 3)

Input Layer.

- Input dimension: 1000
- Operation: Direct feature vector input

Hidden Layers.

- Number of hidden layers: 3
- Hidden dimensions: $[512, 256, 128]$
- Each layer consists of:

- Linear layer
- Batch normalization
- ReLU activation
- Dropout ($p = 0.1$)
- Layer sequence: 1000 \rightarrow 512 \rightarrow 256 \rightarrow 128

Output Layer.

- Final hidden representation \rightarrow Linear(128, 2) for binary prediction

Initialization.

- Linear layers: Xavier uniform initialization
- Bias terms: Zero initialization

Training Configuration.

- Optimizer: Adam
- Learning rate: 1×10^{-4} (for MRSA vs MSSA), 5×10^{-6} for (Penicillin vs. Meropenem)
- Batch size: 256 (for MRSA vs MSSA), 64 for (Penicillin vs. Meropenem)
- Epochs: 8 per permutation
- Loss: CrossEntropyLoss
- Dropout: 0.1

1.4. Improved MLP Architecture

Model Overview - The *Improved MLP* is an enhanced Multi-Layer Perceptron designed for binary classification tasks with high-dimensional input features. It employs derivative feature extraction to capture first and second-order derivatives of the input signal, followed by residual feed-forward blocks with layer normalization for improved gradient flow and feature learning. (used in Table 3)

Feature Extraction.

- Input dimension: 1000
- Derivative computation:
 - First derivative: Conv1d($x, [-1, 1]$) producing dx of length $L - 1$
 - Second derivative: Conv1d($x, [1, -2, 1]$) producing d^2x of length $L - 2$
 - Original signal: center-cropped to length $L - 2$ to match d^2x
- Feature concatenation: $[x_{\text{cropped}}, dx_{\text{cropped}}, d^2x]$ flattened to $3 \times (L - 2) = 2994$ dimensions

Residual Feed-Forward Blocks.

- Number of blocks: 3 (matching hidden dimensions)
- Hidden dimensions: [512, 256, 128]
- Each *ResidualFFN* block consists of:
 - Pre-normalization (LayerNorm)
 - Linear layer
 - GELU activation
 - Dropout ($p = 0.2$)
 - Second linear layer
 - Residual connection (with projection when dimensions differ)
- Block sequence: 2994 \rightarrow 512 \rightarrow 256 \rightarrow 128

Classification Head.

- Layer normalization: LayerNorm(128)
- Final linear layer: Linear(128, 2) for binary prediction

Initialization.

- Linear layers: Xavier uniform initialization
- Bias terms: Zero initialization
- Projection layers (skip connections): Xavier uniform initialization

Training Configuration.

- Optimizer: Adam
- Learning rate: 1×10^{-4} (for MRSA vs MSSA), 1×10^{-5} for (Penicillin vs. Meropenem)
- Batch size: 256
- Epochs: 10 per experiment or permutation
- Loss: CrossEntropyLoss
- Dropout: 0.2 (for MRSA vs MSSA), 0.5 for (Penicillin vs. Meropenem)
- Weight decay: 1×10^{-3}

2. Results Across Five Experimental Replications

Table 5. Evaluation on controlled benchmarks using LightCNN and LightViT architectures. Observed accuracy (Obs. Acc.) is computed under true label assignments, and lower p -values indicate stronger causal evidence against the null. Reported values are expressed as mean \pm standard deviation across 5 randomized replications. (Here, $p_{\min} = 0.0040$ for both experiments)

Architecture	Dataset	Treatment Level	Obs. Acc. (%)	p -value
LightCNN	Rotated MNIST	0°	98.58 \pm 0.15	0.8560 \pm 0.1080
		5°	99.21 \pm 0.57	0.3600 \pm 0.4760
		10°	99.64 \pm 0.20	0.0480 \pm 0.0920
		15°	99.71 \pm 0.05	0.0080 \pm 0.0000
		20°	99.73 \pm 0.05	0.0080 \pm 0.0040
		25°	99.76 \pm 0.02	0.0040 \pm 0.0000
		30°	99.77 \pm 0.04	0.0080 \pm 0.0000
		45°	99.88 \pm 0.03	0.0040 \pm 0.0040
		60°	99.92 \pm 0.02	0.0040 \pm 0.0040
		90°	99.92 \pm 0.02	0.0040 \pm 0.0040
LightCNN	Colored FashionMNIST	$\mu_R = 0.50$	93.67 \pm 0.01	0.4080 \pm 0.0048
		$\mu_R = 0.55$	94.88 \pm 0.05	0.1600 \pm 0.0065
		$\mu_R = 0.60$	97.42 \pm 0.16	0.0240 \pm 0.0082
		$\mu_R = 0.65$	99.15 \pm 0.12	0.0080 \pm 0.0040
		$\mu_R = 0.70$	99.82 \pm 0.02	0.0040 \pm 0.0040
		$\mu_R = 0.75$	99.96 \pm 0.02	0.0040 \pm 0.0040
		$\mu_R = 0.80$	100.00 \pm 0.00	0.0040 \pm 0.0040
		$\mu_R = 0.85$	100.00 \pm 0.00	0.0040 \pm 0.0040
		0°	94.72 \pm 1.63	0.6240 \pm 0.2160
		5°	94.17 \pm 2.80	0.6480 \pm 0.2440
LightViT	Rotated MNIST	10°	87.14 \pm 9.56	0.7680 \pm 0.3240
		15°	91.07 \pm 4.02	0.8800 \pm 0.0520
		20°	93.96 \pm 3.21	0.6840 \pm 0.1960
		25°	94.59 \pm 2.80	0.6280 \pm 0.3360
		30°	95.02 \pm 2.19	0.6440 \pm 0.3680
		45°	95.14 \pm 1.88	0.7000 \pm 0.2400
		60°	97.48 \pm 1.13	0.2520 \pm 0.3160
		90°	99.13 \pm 0.22	0.0080 \pm 0.0040
		0°	92.28 \pm 0.03	0.2317 \pm 0.0072
		5°	94.37 \pm 0.13	0.0800 \pm 0.0017
LightViT	Colored FashionMNIST	$\mu_R = 0.60$	97.37 \pm 0.07	0.0128 \pm 0.0016
		$\mu_R = 0.65$	99.10 \pm 0.05	0.0064 \pm 0.0020
		$\mu_R = 0.70$	99.77 \pm 0.02	0.0080 \pm 0.0000
		$\mu_R = 0.75$	99.97 \pm 0.01	0.0072 \pm 0.0040
		$\mu_R = 0.80$	100.00 \pm 0.00	0.0080 \pm 0.0000
		$\mu_R = 0.85$	100.00 \pm 0.00	0.0080 \pm 0.0000

Table 6. Evaluation on the Rotated MNIST benchmark using the UltraLightViT architecture.

Dataset	Treatment	UltraLightViT	
		Acc. (%)	<i>p</i> -value
Rotated MNIST	0°	82.19	0.5880
	5°	83.71	0.4720
	10°	87.76	0.1760
	15°	88.85	0.1040
	20°	89.60	0.0520
	25°	90.65	0.0320
	30°	91.98	0.0160
	45°	93.22	0.0120
	60°	93.15	0.0160
	90°	93.36	0.0040

3. Ablation Study

We observed that the *p*-values on Rotated MNIST (Table 1) were irregular and did not follow the expected progression across rotation angles. We think this may be because our original LightViT model was too strong for the task, producing saturated accuracies and very low permutation variance. To explore this hypothesis, we intentionally under-powered our LightViT backbone, resulting in the simplified UltraTinyViT, and repeated the evaluation and reported them in Table 6.

3.1. UltraTinyViT architecture.

Our UltraTinyViT is a heavily simplified ViT variant compared to the original LightVisionTransformer. First, we use a much smaller backbone: the embedding dimension is reduced from 96 to 16, the number of transformer blocks (depth) from 6 to 1, and the MLP expansion ratio from 4.0 to 2.0. The patch embedding is changed from a patch size of 4 (producing 49 patches arranged in a 7×7 grid) to a patch size of 7 (producing 16 patches in a 4×4 grid), and the convolutional projection is made bias-free. We completely remove the class token and learnable positional embeddings (and thus also positional interpolation and positional dropout) and instead perform simple mean pooling over all patch tokens before classification. The self-attention module is reduced from multi-head attention with three heads, a biased query-key-value projection, an explicit output projection, and dropout, to single-head attention with a bias-free query-key-value projection, no separate output projection, and no attention dropout. The MLP block is similarly simplified: both linear layers are bias-free, the expansion ratio is smaller, and all dropout is removed. Finally, all LayerNorm layers use non-affine normalization (no learnable scale or shift parameters), the classifier head does not include a bias term.

3.2. Observation

As seen in Table 6, the UltraLightViT results on the Rotated MNIST benchmark now exhibit the behavior we would intuitively expect from a well-calibrated causal test. At small rotation angles, the model already achieves high accuracies; however, the corresponding *p*-values also remain high. This combination indicates that, despite good predictive performance, the model has not yet learned a meaningful causal signal, as such accuracies are still compatible with the null distribution under label permutations. As the rotation angle increases, thereby strengthening the applied signal, the accuracies continue to rise while the *p*-values decrease in a smooth, nearly monotonic fashion, reaching their minimum at 90°. This stands in contrast to the earlier LightViT results, where the *p*-values fluctuated irregularly across treatments despite high accuracies. In our view, the UltraLightViT behavior is more interpretable: larger rotation angles make the observed accuracy stand further above the null distribution, resulting in smaller *p*-values and a clearer correspondence between treatment strength and causal significance.

Taken together, these results confirm our earlier hypothesis: the irregular *p*-value behavior in Table 1 was not due to a failure of the causal framework, but rather a consequence of using a model whose capacity was disproportionately high relative to the signal in the Rotated MNIST task. By reducing the model capacity, the permutation variance becomes more expressive, revealing the expected causal pattern. This finding highlights an important practical point of our framework: when a model is overly strong for a given dataset, accuracy alone can obscure the true causal structure, whereas the permutation-based *p*-values remain sensitive to such mismatches and provide a more reliable indicator of whether the model is responding to genuine treatment signals.